

# Pressure-Induced Mott Insulator-to-Metal Transition in van der Waals compound $\text{CoPS}_3$

Takahiro Matsuoka,<sup>1,\*</sup> Rahul Rao,<sup>2</sup> Michael A. Susner,<sup>2</sup> Benjamin S. Conner,<sup>3,4</sup> Dongzhou Zhang,<sup>5,6</sup> and David Mandrus<sup>1,7,8,†</sup>

<sup>1</sup>*Department of Materials Science and Engineering,  
University of Tennessee, Knoxville, TN 37996, USA*

<sup>2</sup>*Materials and Manufacturing Directorate, Air Force Research Laboratory,  
Wright-Patterson Air Force Base, OH 45433, USA*

<sup>3</sup>*Sensors Directorate, Air Force Research Laboratory,  
Wright-Patterson Air Force Base, OH 45433, USA*

<sup>4</sup>*National Research Council, Washington D.C. 20001, USA*

<sup>5</sup>*Hawaii Institute of Geophysics and Planetology,  
University of Hawaii at Manoa, 1680 East-West Road, Honolulu, HI 96822*

<sup>6</sup>*GSECARS, University of Chicago, 9700 S Cass Ave, Argonne, IL 60439*

<sup>7</sup>*Department of Physics and Astronomy, University of Tennessee, Knoxville, TN 37996, USA*

<sup>8</sup>*Materials Science and Technology Division, Oak Ridge National Laboratory, Oak Ridge, TN 37831, USA*  
(Dated: November 16, 2022)

We have studied the Mott insulator-to-metal transition (IMT) and concomitant evolution of structural properties under high pressure in the van der Waals compound  $\text{CoPS}_3$  through *in-situ* electrical resistance, Hall effect, magnetoresistance, X-ray diffraction, and Raman scattering measurements.  $\text{CoPS}_3$ , a native antiferromagnet at 122 K under ambient conditions, exhibits an IMT at 7 GPa, coinciding with a  $C2/m \rightarrow P\bar{3}$  structural transformation and a 2.4% reduction in the volume per formula unit, indicative of a Mott transition. This metallic  $\text{CoPS}_3$  observed under high pressure is a hole-dominant conductor with multiple conduction bands. The linear magnetoresistance (LMR), as well as the small volume collapse at the IMT, suggests the incomplete high-spin  $\rightarrow$  low-spin transition in the metallic phase. Thus, the metallic  $\text{CoPS}_3$  may possess an inhomogeneous magnetic moment distribution and short-range magnetic ordering (SRO). By revealing the high-pressure phase and electrical transport property of  $\text{CoPS}_3$ , this report summarizes the comprehensive phase diagram of  $\text{MPS}_3$  ( $M = \text{V, Mn, Fe, Co, Ni, and Cd}$ ) that metallize via Mott transition.

## I. INTRODUCTION

The  $\text{MPS}_3$  ( $M = \text{V, Mn, Fe, Co, Ni, and Cd}$ ) compounds form a family of quasi-two-dimensional (2D) van der Waals compounds. They are isostructural in a monoclinic  $C2/m$  symmetry, with individual lamellae composed of slightly distorted octahedral sites circumscribed by the S atoms bordering the van der Waals gap which are, in turn, arranged in a honeycomb lattice. Of the octahedra,  $2/3$  can be described as a  $+2$  metal cation in an  $\text{MS}_6$  cage. The remaining  $1/3$  of the octahedra are filled with P-P dimers that form a  $[\text{P}_2\text{S}_6]^{4-}$  anionic sublattice which charge balances the aforementioned metal cations. The anionic sublattice is common to all of these compounds; the cations in turn impart the various functionalities native to these systems, including magnetism [1, 2]. These individual lamellae are bonded together by weak van Waals forces, thus creating an overall micaceous structure. In this particular subset of the metal thiophosphate family, all compounds form a Mott insulating state at low temperatures and exhibit 2D antiferromagnetic (AFM) behavior, excepting, of course, for the Cd which in the  $+2$  oxidation state has a closed  $d$ -shell [3–7]. The

2D magnetism exhibited in these materials has attracted recent attention due to the ability to study the effects of extreme anisotropy in low dimensions. The  $\text{MPS}_3$  family thus offers an enticing materials platform to study novel magnetic phenomena in low-dimensional materials in addition to the promise for applications in magnetic and spintronic devices because they can be exfoliated down to thin films [8–11]. Therefore, elucidating the physical properties of these interesting 2D magnetic materials is of vital interest for future applications. In particular, it is especially important to consider the structural and magnetic changes induced by imparting pressure to these materials.

External pressure is an effective perturbation tool because van der Waals compounds are highly compressible, especially in the inter-layer direction. Thus far, the structural, magnetic, and electronic evolutions of  $\text{MPS}_3$  under compression have been extensively studied for the thiophosphates  $\text{MPS}_3$  ( $M = \text{V, Mn, Fe, Ni, Cd}$ ) and their analogous selenophosphate counterparts  $\text{MPSe}_3$ . Researchers have commonly observed that these materials exhibit an insulator-to-metal transition (IMT) at high pressures (12–28 GPa) [7, 12–17]. Additionally, spin-crossover (high to low-spin state) occurs in  $\text{FePS}_3$  ( $\text{FePSe}_3$ ) and  $\text{MnPS}_3$  ( $\text{MnPSe}_3$ ) concomitantly with the IMT [13, 14]. Finally,  $\text{FePSe}_3$  becomes superconducting when high pressures are imparted to it, with a super-

\* tmatsuok@utk.edu

† dmandrus@utk.edu

conducting transition temperature of 2.5 K at 9 GPa (increasing to 5.5 K at 30 GPa) [14]. Evidence for an IMT has also been reported recently in a bimetallic metal thiophosphate, Cu-deficient  $\text{CuInP}_2\text{S}_6$  [18]. Clearly, in metal thio- and selenophosphates, pressure-driven structural phase transitions are critical as drivers of new states of matter with the potential to host emergent properties. External pressure induces inter-layer sliding transitions, followed by a 10-20% volume collapse across the IMT at room temperature [4, 12, 13, 15, 19, 20]. Other transitions can be more subtle. For example, the  $\text{MPS}_3$  ( $M = \text{Fe}, \text{Mn}$ ) and  $\text{V}_{0.9}\text{PS}_3$  compounds change from  $C2/m$  to a  $C2/m$  with a different monoclinic angle ( $\beta$ ) or a trigonal  $P\bar{3}1m$ .  $\text{CdPS}_3$  changes from  $C2/m$  to a trigonal  $R\bar{3}$  [20]. As can be imagined for IMTs, bandgap reduction occurs during the compression, accompanied by color changes due to increasing light reflection as the materials become metallic [19]. In previous studies of  $\text{NiPS}_3$ , up to five high-pressure phases have been reported ( $P\bar{3}$ ,  $P\bar{3}m1$ ,  $P3m1$ ,  $P3$ , and  $P1$ ) between ambient pressure and 39 GPa, making this composition unique among these van der Waals gapped magnetic materials [21]. Interestingly, the  $P3m1$  phase is potentially a polar metal [21]. Of course, the atomic, electronic, and magnetic structures in these compounds are all linked.

Focusing on the last of these properties, the trigonal distortion present in the octahedra bounding the metal cations (where the trigonal axis is parallel to the stacking direction) affects the degeneracy of the energy states associated with the octahedral crystal field splitting, thus creating highly anisotropic effects in the magnetism of these compounds [1] that in turn contribute to their interesting behavior. From a structural perspective, the magnetic  $\text{MPS}_3$  or  $\text{MPSe}_3$  compounds which have been studied in detail can be grouped into three main categories. In all compounds, spins are pointed along the  $c$ -axis except for  $\text{NiPS}_3$  and  $\text{CoPS}_3$  where spins are pointed parallel and antiparallel to the  $a$  direction. The first grouping of these magnetic  $\text{MPS}_3$  compounds are  $\text{MnPS}_3$  and  $\text{MnPSe}_3$ ; both of these compounds are co-linear antiferromagnets with propagation vectors of  $\mathbf{q} = [0\ 0\ 0]$  [22–24]. However, for  $\text{MnPS}_3$ , other works state that  $\mathbf{q} = [0\ 1\ 0]$  [5].

The second main grouping contains  $\text{CoPS}_3$  and  $\text{NiPS}_3$ ; both of these materials exhibit propagation vectors of  $\mathbf{q} = [0\ 1\ 0]$  [3, 6]. In the case of  $\text{CoPS}_3$ , though the orientation of the moments are mostly along the  $a$ -axis, a small component is along the  $c$ -axis as well [3]. Finally, the third grouping of these magnetic 2D materials is comprised of the compounds  $\text{FePS}_3$  and  $\text{FePSe}_3$ . The sulfide has been shown to have an incommensurate propagation vector of  $\mathbf{q} = [1/2\ 1/2\ 0.34]$  [25] while the selenide has a vector of  $\mathbf{q} = [1/2\ 0\ 1/2]$  [23, 24]. The careful reader may note that  $\text{V}_{0.8}\text{PS}_3$  [26],  $\text{NiPSe}_3$  [27], and many of the quarternary magnetic compounds [1] have yet to be fully characterized in terms of magnetic structure and may yield fruitful investigations themselves if suitably sized crystals can be synthesized.

To date, the effects of high pressure on  $\text{CoPS}_3$  have not been experimentally reported, probably due to the significant difficulty in the synthesis and single crystal growth of this compound.  $\text{CoPS}_3$  is an antiferromagnet at ambient pressure with a Neel temperature of  $T_N = 122$  K and a Weiss temperature of  $\theta = -116$  K [28]. Its effective moment is  $4.9\ \mu_B$ , slightly larger than the expected value for a pure spin moment of a  $\text{Co}^{2+}$  ( $S = \frac{3}{2}$ ) cation [28], implying some degree of orbital contribution to the magnetization. A first-principles calculation, the only dedicated article to the effects of pressure in  $\text{CoPS}_3$ , predicts a pressure-driven isostructural Mott transition accompanied by a spin-crossover (SCO) [29]. Intriguingly, this theoretical study demonstrates the emergence of ferromagnetic (FM) half metallic states with 100% spin-polarization, which is a long-sought state because of its potential applications with respect to spin-current injection and detection [29].

In the study for new novel physical properties in the  $\text{MPS}_3$  family,  $\text{CoPS}_3$  has been the final missing piece. Comparing and contrasting with its sister compounds should provide better knowledge that contributes to a fuller understanding of the emergent phenomena in the  $\text{MPS}_3$  family under compression.

In this study, we successfully grew large single crystals of  $\text{CoPS}_3$  in general accordance with the method reported in Ref. [3]. This enabled us to perform electrical resistance, Hall effect, magnetoresistance, Raman scattering, and X-ray diffraction (XRD) measurements under high pressures. Our studies reveal an IMT around 7 GPa, coinciding with a  $C2/m \rightarrow$  trigonal structural transformation and a 2.4% reduction in the volume per formula unit, indicative of a Mott transition. The XRD and Raman scattering data also suggest  $P\bar{3}$  symmetry for this metallic trigonal phase. We find, through Hall effect measurements, that the metallic phase is a hole-dominant conductor with multiple conduction bands. The linear magnetic field dependence of the magnetoresistance (LMR), combined with the small volume collapse at the IMT, suggests an incomplete high-spin  $\rightarrow$  low-spin transition in the metallic phase. Thus, metallic  $\text{CoPS}_3$  may possess an inhomogeneous magnetic moment distribution and short-range magnetic ordering. Taking these data on  $\text{CoPS}_3$  in combination with a review of similar effects on related metal thiophosphate materials, we find evidence for the inter-atomic distance, rather than structural symmetry, playing a crucial role in initiating the pressure-induced spin-cross-over and IMT. This report summarizes the comprehensive phase diagram of  $\text{MPS}_3$  that metallize via Mott transition.

## II. EXPERIMENTAL METHOD

We synthesized single crystals of  $\text{CoPS}_3$  using the general procedures outlined in Refs. [1, 3]. Briefly, Co powder (Alfa Aesar Puratronic, 22 mesh, 99.998%, reduced), P chunks (Alfa Aesar Puratronic, 99.999%), and S (Alfa

Aesar Puratronic, 99.9995%) were combined in a near-stoichiometric ratio to form  $\text{CoPS}_3$  together with an appropriate quantity of  $\text{I}_2$  as the vapor transport agent[30] in a sealed quartz ampoule, heated to the reaction temperature, and held there for 4 days. Typical crystals were 4–6 mm in size along the  $a-b$  planes with several exceeding 12 mm. Thicknesses of the crystals were typically < 0.5 mm.

To impart high pressure to our materials, we used diamond anvil cells (DACs) equipped with type-Ia diamond anvils. In Figure 1, we show the experimental setup for the electrical resistance measurements. The culet diameters of the diamond anvils were 500  $\mu\text{m}$  for the transport, 520  $\mu\text{m}$  for XRD, and 500  $\mu\text{m}$  for Raman scattering measurements. The 0.25-mm-thick metal gaskets (stainless steel, SUS310) were pre-indented to 50  $\mu\text{m}$ , and a 200  $\mu\text{m}$  diameter hole (sample chamber) was drilled in the center of the pre-indented area. A layer of compressed diamond powder and epoxy resin mixture insulates the electrical leads [platinum (Pt) film, 5  $\mu\text{m}$  in thickness] from the metal gasket. A small single crystal flake of about 10  $\mu\text{m}$  in thickness was exfoliated from a large single crystal. Then, the flake was shaped to closely match the sample chamber. The single crystals were loaded with the  $a-b$  planes laying on the diamond's flat surface. A pre-compressed sodium chloride (NaCl) flake was placed underneath the sample, serving as a pressure-transmitting medium (PTM) and ensuring that the pressure distribution across the sample was as homogeneous as possible. NaCl is replaced with potassium chloride (KCl) in the XRD experiments. Several tiny ruby chips ( $\text{Cr:Al}_2\text{O}_3$ ) were added together with the samples as a pressure standard [31]. The configuration of the sample and gasket is identical in transport and XRD experiments, except that the electrical leads and insulation layers were not present in the XRD measurements. We performed the transport measurements using a KEITHLEY 2450 source meter to apply current, and two KEITHLEY 2450 nano-voltmeters to sense voltage. In these experiments, the applied currents were 0.1 mA (0–7.4 GPa) and 1 mA (10–16 GPa); the larger current was needed for the metallic state. We used a Quantum Design Physical Property Measurement System (PPMS) to control temperature and magnetic field in the resistance measurements. We estimated the pressures through the R1 fluorescence peak of ruby [31]. For the electrical resistance measurements, we obtained the pressure by averaging the pressure values measured at room temperature before and after each temperature cycle. We ask the reader to note that the actual pressures at low temperatures are thought to be somewhat different from the indicated values.

The high-pressure Raman spectroscopy measurements were conducted in a Merrill-Bassett type diamond anvil cell (DAC with Boehler-Almax anvils. We used a 500  $\mu\text{m}$  culet diamond with a maximum operating pressure of 20 GPa. A  $\text{CoPS}_3$  crystal was loaded on to the diamond within a stainless steel gasket with a 90  $\mu\text{m}$

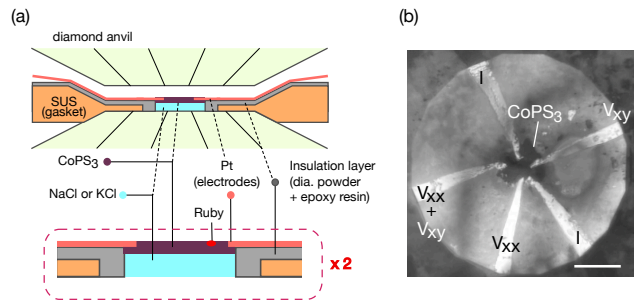


FIG. 1. (color online) The experimental setup for the electrical transport measurements in the DAC. (a) The schematic cross-section of the DAC. (b) The microphotograph of  $\text{CoPS}_3$  at 4.5 GPa, looking at the  $a-b$  plane of  $\text{CoPS}_3$  through a diamond anvil. The scale bar 100  $\mu\text{m}$ . The Pt electrodes labeled I,  $V_{xx}$ , and  $V_{xy}$  are used for applying current, sensing the voltages transverse ( $V_{xy}$ ) and longitudinal ( $V_{xx}$ ) to the current, respectively. The electrode at nine o'clock is used as a 'common' ground in the measurements.

aperture, along with a small ruby crystal as the pressure measurement standard. We then filled the chamber with a 4:1 ratio methanol/ethanol solution which acts as the pressure transmitting medium. Same as the electrical resistance and the XRD measurements, the pressures were estimated through the R1 fluorescence peak of ruby [31]. Room-temperature pressure-dependent Raman spectra were collected with a Renishaw inVia Raman microscope with a 632.8 nm excitation laser focused through a 50 $\times$  magnification long working distance objective lens onto the  $\text{CoPS}_3$  crystal. The pressure was exerted manually through three external screws and Raman spectra were collected with an excitation laser power of  $\sim 1 \mu\text{W}$  to minimize heating. Following the Raman measurements, we performed spectral analysis (in Igor Pro) by normalizing intensities with respect to the diamond Raman peak, followed by a spline baseline subtraction and Lorentzian peak fitting to extract frequencies and linewidths.

We performed XRD measurements at beamline 13BM-C at the Advanced Photon Source (APS), Argonne National Laboratory. The wavelength of the X-ray beam was 0.4340  $\text{\AA}$ , and the beam spot size was 12  $\mu\text{m}$  (H)  $\times$  18  $\mu\text{m}$  (V) in all measurements. We collected diffraction data on a flat panel detector array (Dectris Pilatus 1M-F, pixel size: 172  $\times$  172  $\mu\text{m}^2$ ) in the forward scattering geometry at room temperature. The sample-to-detector distance and the detector tilt were calibrated with the NIST SRM660a  $\text{LaB}_6$  standard. For two-dimensional XRD data reduction, we used Dioptas [32]. Diffraction measurements were taken with the DAC rotated about the horizontal axis ( $\pm 30^\circ$ ) to maximize the number of reflections from the single-crystal like samples.

### III. RESULTS

#### A. Resistance vs. Pressure and Temperature

Fig. 2a shows the pressure dependence of the electrical resistance ( $R_{xx}$ ) and resistivity ( $\rho_{xx}$ ) from CoPS<sub>3</sub> at room temperature without applying external magnetic field. The  $\rho_{xx}$  was calculated using the area/length ratio,  $wt/l$  where  $w = 50 \mu\text{m}$  (#1 and #2) is the width of the sample,  $t = 20 \mu\text{m}$  (#1) and  $10 \mu\text{m}$  (#2) is the thickness, and  $l = 55 \mu\text{m}$  (#1) and  $40 \mu\text{m}$  (#2) is the separation between electrical leads measured before applying pressure. The  $R_{xx}$  decreases into the measurable range of our transport measurement system (maximum  $2 \text{ M}\Omega$ ) above 2 GPa. The  $\rho_{xx}$  shows a significant decrease under compression up to 7 GPa by three orders of magnitude, after which point it abruptly decreases by five further orders of magnitude when applying an additional mere 1 GPa of pressure. Above 8 GPa,  $\rho_{xx}$  becomes almost independent of the external pressure. The similarities in the trends from two independent samples #1 and #2 show good reproducibility of the transport results (Fig. 2a). The insets of Fig. 2a show micrographs of CoPS<sub>3</sub> at 4.5 GPa and 12 GPa observed under epi-illumination. Here we see that the light reflection increases with pressure where the sample at 12 GPa is shiny and comparable to the Pt metal used for the electrical probes, thus indicating a major electronic transition. Note that the shadows in the upper picture are due to the refraction from the diamond while the illumination intensity was kept constant throughout the pressure study.

Upon release of the pressure, the  $\rho_{xx}$  traces back the  $\rho_{xx}$  vs.  $P$  curve of the compression down to 8 GPa. Below 8 GPa, the  $\rho_{xx}$  stays much lower (one to three orders of magnitude) than that of the compression, showing a large hysteresis. However, at 0 GPa the compressed and decompressed lines are extrapolated to merge. This large hysteresis between compression and decompression implies the presence of a first order transition.

To see if there are any temperature dependent resistivity effects, in Fig. 2b (top panel) we show  $\rho_{xx}$  vs.  $T$  at various pressures (Sample #1) without the application of an external magnetic field. The CoPS<sub>3</sub> exhibits insulating or semiconducting behavior at 7.4 GPa and also exhibits a negative slope ( $d\rho_{xx}/dT$ ). The origin of the hump at 7.4 GPa and 50 K is as of yet unknown. Above 10 GPa,  $d\rho_{xx}/dT$  becomes positive along the entirety of the probed temperature range, thus implying that CoPS<sub>3</sub> is metallic under these pressures. We see no superconducting transition in the measured temperature range, down to 2 K for metallic CoPS<sub>3</sub> (bottom panel of Fig. 2b). When we plot the  $\rho$  as a function of  $T^2$  (inset in the bottom panel of Fig. 2b), we see that  $d\rho_{xx}/dT$  fits the Fermi-liquid theory at temperatures below 20 K. Thus, we conclude that CoPS<sub>3</sub> exhibits a pressure-induced IMT around 7 GPa. When the pressure is released to 3.5 GPa, CoPS<sub>3</sub> reverts back to an insulator (Fig. 2a).

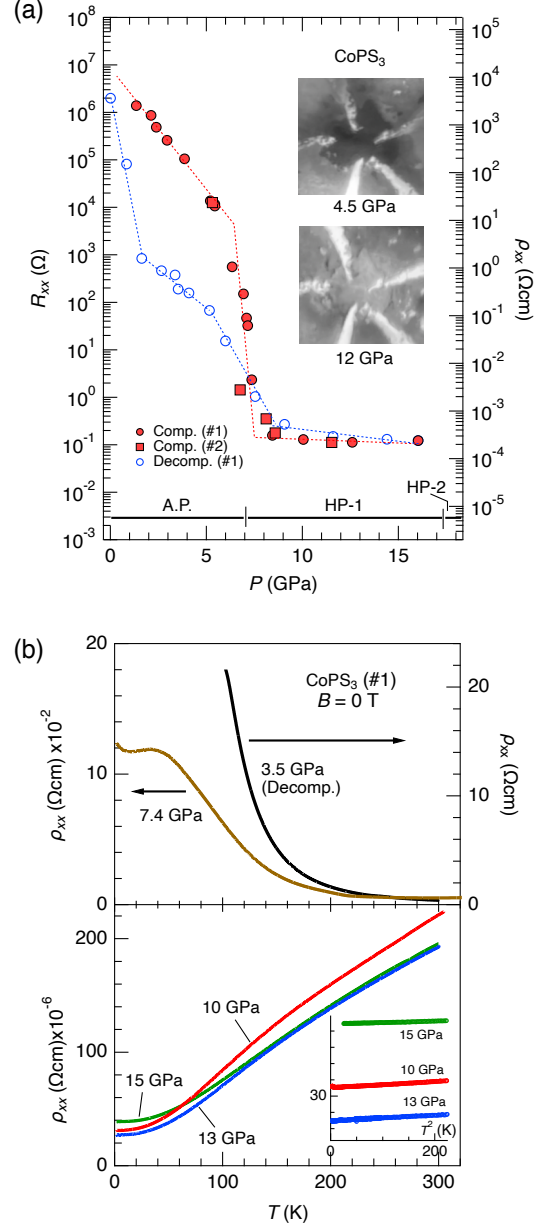


FIG. 2. (color online) (a)  $R_{xx}$  and  $\rho_{xx}$  vs.  $P$  at room temperature. The results of two independent measurements are plotted for the compression and decompression processes. The dotted lines overlapping the open and closed markers are guides for eyes. The vertical and horizontal solid lines indicate the observed structural phase diagram confirmed by our XRD and Raman scattering measurements, below. The inset pictures show sample #1 in A.P.-phase and HP-I phase. (b)  $\rho_{xx}$  vs.  $T$  at pressures obtained for Sample #1 without an external magnetic field. All data plots are taken on warming. The inset figure plots the  $\rho_{xx}$  as a function of  $T^2$ .

## B. XRD

Figure 3a displays the representative XRD patterns of CoPS<sub>3</sub> at 0.5 and 17 GPa. We note that the observed XRD patterns are affected by the orientation reflecting the initial geometry of the single crystal when loaded in the DAC. In our measurements, the *a-b*-plane of the layered structure is perpendicular to the X-ray beam. Although we rotated the DAC as much as allowed by the beamline instruments and the DAC opening angle, the diffraction peaks from (*hkl*) with large *l* (>2) are invisible, limiting the number of peaks. Additionally, the single crystal partially broke into several pieces during compression. Therefore, the relative intensity between the diffraction peaks is inaccurate because the obtained XRD results are not in the form of even intensity powder rings. See the Supplementary Material for the XRD image recorded on a detector [33]. At ambient pressure (A.P.), the XRD peak positions agree well with the previously reported monoclinic *C2/m* (*a* = 5.844(1) Å, *b* = 10.127(1) Å, *c* = 6.562(4) Å,  $\beta$  = 107.04(2)°) [3]. At 17 GPa, we can index the XRD pattern to a trigonal structure with lattice parameters *a* = *b* = 5.570(5) Å, *c* = 5.13(2) Å. We name the high-pressure trigonal phase HP-I in this report. We also note that a *C2/m* structure can be a candidate, keeping the *a*, *b*, and *c* values similar to 6.6 GPa, but with a  $\beta \sim 90^\circ$ . However, a trigonal unit cell gives better least-square fitting results.

In Figure 3b we show the pressure dependencies of volume per formula unit ( $V_{f.u.}$ ) and the lattice parameters, *a*, *b*, and *c*. The  $V_{f.u.}$  is obtained by dividing a unit cell volume by the number of CoPS<sub>3</sub> units *Z* = 2. For the comparison between A.P. and HP-I, we reduce the trigonal unit cell to a monoclinic unit cell ( $\beta = 90^\circ$ ) using the relation  $b_{mono.} = 2a_{tri.} = 2a_{mono.} \times \cos 30^\circ$ . In agreement with the electrical transport measurements, the structure changes from A.P. (*C2/m*) to HP-I at 7 GPa. At the structural transformation, the  $V_{f.u.}$  abruptly decreases by 2.4% (84.690 → 82.269 Å<sup>3</sup>) at 7 GPa. In addition, all the lattice parameters *a*, *b*, and *c* show a sharp discontinuity due to the reduction in volume above 7 GPa, with *c* exhibiting the largest reduction ( $\Delta c = 1.4$  Å). On decompression, the HP-I phase remains down to 2 GPa upon the release of pressure, displaying a large hysteresis.

We note that a Mott transition is generally accompanied by a volume collapse. For the isostructural MPS<sub>3</sub> (*M* = Fe, Mn), a volume collapse by 10-20% has been commonly observed simultaneously with a spin-crossover (SCO) [13–15]. This study has not performed a direct measurement, such as X-ray absorption spectroscopy and Mössbauer spectroscopy, to investigate the electronic configuration of Co. However, from the observed volume collapse and from making comparisons to similar materials such as FePS<sub>3</sub> and MnPS<sub>3</sub>, it is reasonable to conclude that CoPS<sub>3</sub> exhibits the Mott-IMT at 7 GPa, possibly accompanied by a spin-cross over ( $S = 3/2 \rightarrow 1/2$ ).

We note that the observed volume reduction of CoPS<sub>3</sub> (2.4%) is much smaller than that observed for MnPS<sub>3</sub>

(19.7%) and FePS<sub>3</sub> (10.6%) [13–15]. The ionic radii of high-spin (HS) and low-spin (LS) Co<sup>2+</sup> ions are 0.75 Å and 0.63 Å [34], respectively. The HS → LS radius reduction is thus 16% which is bigger than that of Mn<sup>2+</sup> (HS: 0.81 Å, LS: 0.70 Å, 13.7%) and smaller than Fe<sup>2+</sup> (HS: 0.76 Å, LS: 0.66 Å, 19.2%) [34]. Thus, the small volume reduction of CoPS<sub>3</sub> cannot be explained simply by the difference between HS and LS radii. We discuss the subject in relation to the incomplete SCO across the A.P. → HP-I. Pressure enhances the charge fluctuation in metal ions, promoting the HS → LS cross over [13, 14, 29, 35]. Remarkably, the theoretical study predicts that the magnetic moment in CoPS<sub>3</sub> is much more robust than Fe<sup>2+</sup> and Mn<sup>2+</sup> ions under pressure [29]. Above 12.5 GPa, the CoPS<sub>3</sub> in either the  $R\bar{3}$  or *C2/m* ( $\beta \sim 90^\circ$ ) phases is FM, and the magnetic moments of Co<sup>2+</sup> ions decrease significantly with increasing pressure but do not achieve  $S = 1/2$  even up to 50 GPa [29]. This is in sharp contrast to FePS<sub>3</sub> and FePS<sub>3</sub> that complete the SCO of Mn<sup>2+</sup> ( $S = \frac{5}{2} \rightarrow \frac{1}{2}$ ) and Fe<sup>2+</sup> ( $S = 2 \rightarrow 0$ ) in a narrow pressure range around 2 GPa [13, 14]. As discussed later, and summarized in Table 1, the inter-atomic distance plays a bigger role than the structure symmetry with respect to the initiation of the Mott transition. Although the theoretically predicted crystal structure differs from the one which we have experimentally determined, the prediction of the robust magnetic moments of Co<sup>2+</sup> in HP-I below 15 GPa can be considered to be confirmed. The HP-I of CoPS<sub>3</sub> possibly is in the middle of SCO and possess a HS/LS mixed state.

## C. Raman scattering

To obtain further insights into changes to the symmetry of the crystal structure upon compression, we performed pressure-dependent Raman scattering measurements. Fig. 4a displays the evolution of the Raman spectra from CoPS<sub>3</sub> under quasi-hydrostatic compression at room temperature. Based on the previous theoretical and experimental reports, we anticipate eight Raman active modes ( $5E_g + 3A_g$ ) for bulk CoPS<sub>3</sub> at room temperature [36]. At pressures below 6.7 GPa (in the stability region of *C2/m*), we observe all eight peaks in agreement with the previous reports [36]. The peak at 110 cm<sup>-1</sup> is not observed at ambient pressure (Atm.), but becomes visible above 1.2 GPa, suggesting that a preferential alignment of layers could cause this peak to be more prominent at higher pressures. Up to 6.7 GPa, all the peaks blueshift in frequency with increasing pressure as expected for phonon modes under compression. Interestingly, between 6.7 GPa and 7.5 GPa, the Raman spectrum changes abruptly with the loss of peaks and the appearance of new peaks (Fig. 4a and 4b). Accompanied by the Raman spectral change, the sample becomes lighter in color and more reflective under epillumination (Fig. 4a), in agreement with the visible observations during our transport measurements (Fig. 2a).



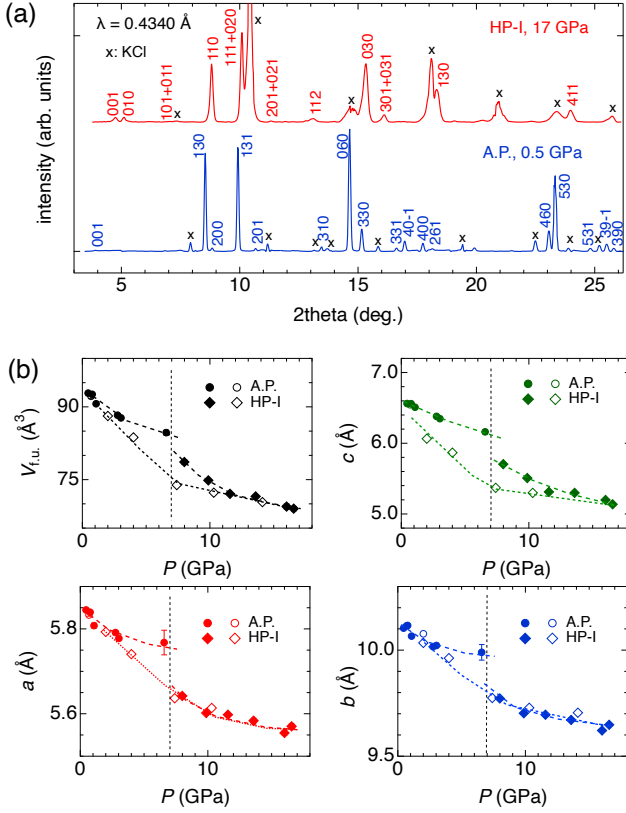


FIG. 3. (color online) Structure analysis of CoPS<sub>3</sub> by XRD under pressure. (a) XRD patterns collected from the A.P. (0.5 GPa) and HP-I (17 GPa) phases. KCl changes from B1 type to B2 type structure at 2 GPa. (b) Pressure evolution of  $V_{f.u.}$  and lattice parameters. To compare the lattice parameters between the phases, the trigonal structure of HP-I is reduced to a monoclinic lattice with the monoclinic angle  $\beta = 90^\circ$ . The open and closed data points indicate compression and decompression processes, respectively. The broken and dashed curves are guides for eyes. The vertical dotted line indicates the structural phase boundary.

The abrupt changes in the Raman spectra and reflectivity give further evidence of the A.P.  $\rightarrow$  HP-I structural change coinciding with the ITM transition. Similar to what we see in the transport measurements, the transition in the Raman spectra takes place within a narrow pressure range of 0.8 GPa, strongly suggesting the absence of an intermediate phase between the A.P. and HP-I phases. At the highest pressure (18.7 GPa), all peaks diminish significantly and are replaced by a broad peak between 300-400  $\text{cm}^{-1}$ , except for the peak near 120  $\text{cm}^{-1}$  which persists throughout the whole pressure study. We conclude that the crystal structure changes to another high-pressure phase above 16.7 GPa, and we name it HP-II.

The left panel in Fig. 4b shows the pressure-dependent frequencies of the Raman peaks in the range of 100 – 620  $\text{cm}^{-1}$ . The transition from the A.P.-phase to the HP-I phase is denoted by the dashed vertical line. The right

panel in Fig. 4b shows a magnified view of the pressure-dependent peak frequencies in the A.P.-phase. The pressure coefficient of peak shift ( $\text{cm}^{-1}/\text{GPa}$ ) shown in the right panel is obtained by linear fitting each mode. Based on the previous literature, we assign the peak  $P_4$  near 245  $\text{cm}^{-1}$  to the out-of-plane bending ( $A_{1g}$ ) of  $\text{P}_2\text{S}_6^{4-}$  dimer units. It has the highest pressure coefficient, reflecting the large compressibility in the  $c$ -axis (Fig. 3b) [36].  $P_8$  near 560  $\text{cm}^{-1}$  is the out-of plane stretching of P-P dimer ( $E_g$ ) [36]. The peak shows a sharp increase in the frequency at the starting of compression. On the other hand,  $P_6$  near 380  $\text{cm}^{-1}$  representing in-plane stretching of  $\text{P}_2\text{S}_6^{4-}$  units ( $A_{1g}$ ) has the lowest pressure coefficient [36]. Overall, our Raman data shows that compression affects out-of-plane phonon modes to a greater degree than in-plane modes.

Next, we try to understand the  $C2/m \rightarrow$  HP-I transition. We first track the peak frequency changes across the A.P.  $\rightarrow$  HP-I critical pressure.  $P_1$  near 115  $\text{cm}^{-1}$  (complex vibrations along all three axes of Co and S,  $E_g$ ) blue shifts with pressure up to 7 GPa, above which it redshifts in frequency (labeled  $P_{1'}$  in Fig. 4b).  $P_2$  near 145  $\text{cm}^{-1}$  (in-plane Co-Co stretching,  $E_g$ ) and  $P_3$  near 238  $\text{cm}^{-1}$  (out-of-plane stretching of  $\text{P}_2\text{S}_6^{4-}$ ,  $E_g$ ) behave similarly to  $P_1$ , blueshifting up to 7 GPa, followed by slight discontinuities and are designated as  $P_{2'}$  and  $P_{3'}$  in the HP-I phase, respectively.  $P_4$  near 240  $\text{cm}^{-1}$  merges with  $P_5$  near 280  $\text{cm}^{-1}$  (in-plane S-S vibration in  $\text{P}_2\text{S}_6^{4-}$  units,  $E_g$ ) up to 7 GPa. In the HP-I phase, the merged peak is designated as  $P_{4',5'}$  near 300  $\text{cm}^{-1}$ .  $P_6$  near 380  $\text{cm}^{-1}$  (in-plane S-S vibration,  $A_{1g}$ ) exhibits a sharp discontinuity across the phase transition and appears at a lower frequency 400  $\text{cm}^{-1}$  (labeled as  $P_{6'}$  in HP-I).  $P_7$  near 545  $\text{cm}^{-1}$  (complex stretching mode of  $\text{P}_2\text{S}_6^{4-}$ ,  $E_g$ ) and  $P_8$  come closer up to 7 GPa. Across the critical pressure, these peaks disappear and the highest frequency peak in HP-I appears at a much lower frequency 510  $\text{cm}^{-1}$ , designated as  $P_{7',8'}$  in Fig. 4b. The lowering of peak frequencies across a phase transition often occurs when the crystal structure changes under pressure. This is because the system relaxes its inter-atomic bonds through the structural change, lowering the total energy compared to its preceding structure at the same pressure. The Raman spectral data in Figure 4 show that all eight observed Raman peaks from CoPS<sub>3</sub> exhibit discontinuities in frequencies above 7 GPa and are accompanied by the appearance of three new peaks ( $P_A$ ,  $P_B$  and  $P_C$ ) across the A.P.  $\rightarrow$  HP-I transition. Our observations therefore provide clear evidence for both increasing and decreasing symmetry. Our XRD and electrical transport experiments suggest the A.P.  $\rightarrow$  HP-I is a first-order transition. Therefore, all our measurements suggest that the initial and final space groups do not have a simple group  $\leftrightarrow$  subgroup relationship.

We first consider the evidence for increased symmetry. As mentioned above, some of the Raman peaks merge with increasing pressure up to 7 GPa ( $P_4+P_5 \rightarrow P_{4',5'}$ , and  $P_7+P_8 \rightarrow P_{7',8'}$ ). This means that in addition to

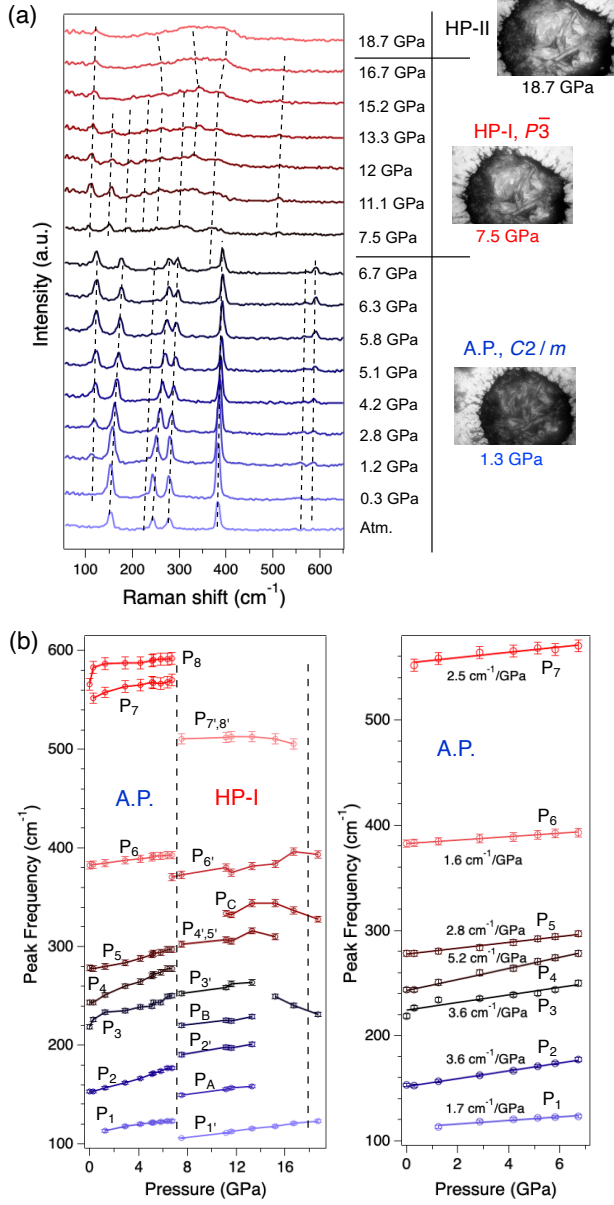


FIG. 4. (color online) Raman scattering measurement results of  $\text{CoPS}_3$  under pressures. (a) The pressure evolution of the Raman scattering spectra at ambient temperature. The dashed lines are the guide for the eyes. Horizontal lines are structural phase boundaries derived from the spectral changes. (b-left) Pressure dependencies of the Raman scattering peaks. Dashed vertical lines show the structural phase boundaries. (b-right) The close-up view of the left panel between 100 and 580  $\text{cm}^{-1}$ .

the mirror planes, axial glides, inversion centers, two-fold rotations, and the two-fold screw axes that characterize the  $C2/m$  space group, the system gains additional symmetry elements across 7 GPa. Examination of the  $C2/m$  group  $\leftrightarrow$  supergroup relationships provides several higher symmetry candidates such as  $P\bar{3}1m$ ,  $P\bar{3}m1$ , and  $Cmmm$ . Since our XRD results suggests a trigonal structure, we

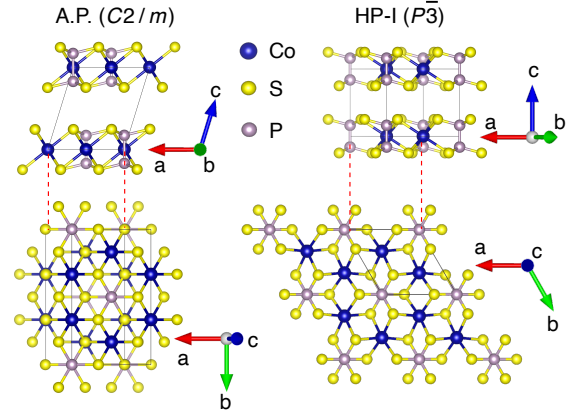


FIG. 5. (color online) The crystal structure of A.P.-phase ( $C2/m$ ) and the suggested  $P\bar{3}$  structure for HP-I phase visualized using VESTA[37].

can immediately exclude  $Cmmm$ . The symmetry tree shown in the Supplemental Material of Ref. [21] summarizes the subgroup/supergroup symmetry relations relevant to the  $\text{MPS}_3$  family of compounds.

Next, we investigate the evidence for symmetry breaking, as signaled by the appearance of the new peaks. The newly emergent peak  $P_A$  (near 140  $\text{cm}^{-1}$ ) in the HP-I phase indicates the rise of the out-of-phase intralayer Co translational mode.  $P_B$  and  $P_C$  are considered to be related to the S-S vibrations from their corresponding frequencies of peaks in the AP phase. To unravel how these modes correspond to the change in crystal symmetry across the critical pressure, we need to consider the relevant mode displacement patterns and how they impact different symmetry elements. These include some of the newly established symmetry elements of  $P\bar{3}1m$  and  $P\bar{3}m1$ , such as axial glide planes, two-fold rotations, and two-fold screw axes. Therefore, candidate subgroups include  $P\bar{3}1m$ ,  $P\bar{3}$ ,  $P\bar{3}m1$ , and  $P312$ . In the Raman spectra, we do not see a large increase in the overall number of peaks, suggesting the retention of the inversion center. Of the four candidate subgroups of  $P\bar{3}1m$  and  $P\bar{3}m1$ ,  $P\bar{3}$  retains the inversion center. We, therefore, suggest that the structure transforms from  $C2/m$  to  $P\bar{3}$  above 7 GPa.

In Figure 5 we summarize the crystal structures of  $\text{CoPS}_3$  in the A.P. and HP-I phases. The  $C2/m$  structure for the A.P.-phase was taken from ref. [3]. Note that the atomic positions in the  $P\bar{3}$  structure model was not refined because we did not perform Rietveld refinement due to the above-mentioned limitation in the obtained XRD data [33].

#### D. Transverse transport measurements

Now that we have confirmed the existence of a new, metallic phase at high pressure in  $\text{CoPS}_3$ , we turn our attention to its electronic properties. Transverse trans-

port measurements, including Hall resistance (HR) and magnetoresistance (MR), are essential probes because it gives us information about the Fermi surface [38]. Fig. 6a and Fig. 6b display the Hall resistivity ( $\rho_{xy}$ ) and MR ( $\Delta\rho_{xx}(B)/\rho_{xx}(0)$ ) at 10, 13, and 15 GPa and temperatures ranging from 1.8-160 K. The  $\rho_{xy}$  shows positive and mostly linear field dependence at all temperatures and pressures (Fig. 6a). Additionally, it does not saturate at the highest field (9 T) of the measurements. We also notice that  $\Delta\rho_{xx}(B)/\rho_{xx}(0)$  exhibits a positive and linear magnetic field dependence (linear magnetoresistance: LMR) at all pressures and temperatures (Fig. 6b). If a material is FM, the anomalous Hall effect is anticipated with a saturation at a high-field. Our transverse transport data thus indicates that CoPS<sub>3</sub> is not FM. However, it is likely that CoPS<sub>3</sub> is a hole-dominant conductor that requires a multiple-conduction band model.

Generally, a multi-band analysis based on a semi-classical description utilizes information such as carrier density and mobility on the Fermi surface from the HR and MR data. However, the obtained results tend to become ambiguous because of hypothesizing the number of carrier types. The LMR in this study makes the analysis even more complicated because it is far from the quadratic behavior anticipated by a semi-classical description that is discussed below (Fig. 6b). Here, we employ a simple one-band model analysis and estimate the orders of density ( $n_{e,av.}$ ) and mobility ( $\mu_{e,av.}$ ), on average, for all carriers. From the relation  $1/eR_H = n_{e,av.}$ , the Hall coefficient ( $R_H$ ) and the electron charge ( $e$ ) provide the estimation  $n_{e,av.} = 1.41 \times 10^{21} \text{ cm}^{-3}$  at 10 GPa and 1.8 K. This value is slightly smaller than that a Hall effect measurement expects for general metals ( $10^{22} \text{ cm}^{-3}$ ). Using the relation  $\sigma = \mu_{e,av.} n_{e,av.}$ , the  $\mu_{e,av.} = 138 \text{ cm}^2 \text{ V}^{-1} \text{ s}^{-1}$  can be extracted, where  $\sigma$  is a conductivity. The  $n_{e,av}$  and  $\mu_{e,av}$  are within the range of  $1.4\text{-}2.9 \times 10^{21} \text{ cm}^{-3}$  and  $55\text{-}138 \text{ cm}^2 \text{ V}^{-1} \text{ s}^{-1}$  at 2 K for all pressures, respectively.

In the following, we discuss the observed LMR (Figs. 6b and 6c). Contrary to the experimental observations, the semi-classical model predicts that the  $\rho_{xx}$  evolves quadratically with magnetic field, saturating at high fields if the hole and electron densities are not compensated [39, 40]. At the low-field limit,  $\omega_c \tau \ll 2\pi$ , where  $\omega_c$  is the cyclotron frequency and  $\tau$  is the relaxation time, the leading term in  $\rho_{xx}$  becomes  $\Delta\rho = \rho(B) - \rho(B=0) \sim H^2$  due to Onsager reciprocity relation, which requires  $\sigma_{ij}(\mathbf{B}) = \sigma_{ji}(-\mathbf{B})$  [39, 40]. The  $\rho_{xx}$  of CoPS<sub>3</sub> evolves almost linearly with the field contrary to the semi-classical description. The LMR is observable down to low fields: 0.7 T at 10 GPa, 2 T at 13 GPa, and 3 T at 15 GPa (Fig. 6c) followed by the asymptotic curves approaching zero near zero field. Elevated temperature suppresses the increase of the  $\rho_{xx}$  vs.  $B$  curves. At higher pressures, the parabolic shape in the  $\rho_{xx}$  vs.  $B$  becomes more obvious at lower fields. To obtain further insight into the linear term in the  $\rho_{xx}$  vs.  $B$  relation, we adopt a phenomenological approach to disentangle these components, fitting

the measured MR as  $\rho_{xx}(H, \text{various } T) = \rho_{xx}(T, H=0) + A(T)H + B(T)H^2$ . We note that this procedure is only valid to a magnitude of  $\Delta\rho$  and is relatively small where the quadratic component is clearly visible. Thus, we perform the fitting below 4 T. Fig. 6d plots  $A(T)H$  and  $B(T)H^2$  as a function of temperature to 160 K. By comparison,  $A(T)$  saturates at low temperature below 10 K.  $B(T)$  does not change appreciably over a wide range of temperatures.

Next, we try to discern the source responsible for LMR and thereby obtain insights into the electronic configuration in CoPS<sub>3</sub>. LMR has been observed in a growing number of novel materials including topological insulators (TIs) [41–46], Dirac [47–50] and Weyl semimetals [51, 52], silver chalcogenides [53, 54], charge-density wave (CDW) and spin-density wave (SDW) systems [55, 56], and quasi two-dimensional electron gas systems [45, 57]. At the high-field limit  $\omega_c \tau \gg 2\pi$ , the extreme quantum limit, there have been several suggested electronic and geometric mechanisms that satisfy the criteria for a quantum LMR. The first is the occurrence of special features on the Fermi surface, such as sufficiently low electron density to permit condensation of the electrons into the lowest spin-split Landau level [58], linear dispersion from a Dirac cone with infinitesimally small carrier mass [59], Umklapp scattering [60], and magnetic breakdown [61]. The second is principally geometric in nature, such as an average over a combination of open and closed electron trajectories in polycrystals [40], guiding center diffusion in weak disorder [62], or strong mobility fluctuations due to irregular current paths from a strongly inhomogeneous medium or conductive grain boundaries [53, 63, 64]. LMR is often invoked as evidence for some exotic quasiparticles in materials.

On the other hand, the fluctuations of density and spin have been suggested as a universal mechanism. The density fluctuations provide an inhomogeneous distribution of charge concentration and affect the conduction carrier path, admixing the HR component with MR [57, 59]. Even a small fluctuation severely influences the  $\rho_{xx}$  in high-mobility materials with a low-mean carrier density where the longitudinal resistivity is small and the Hall voltage rises steeply with increasing field [57, 64]. Similarly to the density fluctuation, the LMR due to the magnetic disorder has been observed for several 3d ferromagnets and FeSe [65, 66]. Another mechanism follows from the study of LMR in CDW and SDW containing materials [56]. Here, the conduction carriers turn the sharp corner of an orbital on the partially gapped electron- and hole-like Fermi surface, creating wandering current paths and the resultant cross-over from quadratic to linear behavior [56]. Those three from their nature can be applicable to the LMR to lower-field limit  $\omega_c \tau \ll 2\pi$ .

To examine the suggested mechanisms, we first estimate an average for all carriers  $\omega_c \tau = B/\rho n e c = 2.75 \times 10^{-2}$  at 2 T (10 GPa, 1.8 K) for CoPS<sub>3</sub>. The criteria for quantum LMR ( $\omega_c \tau \gg 2\pi$ ) (Ref. [59]) are thus not satisfied under our measurement conditions. Addition-



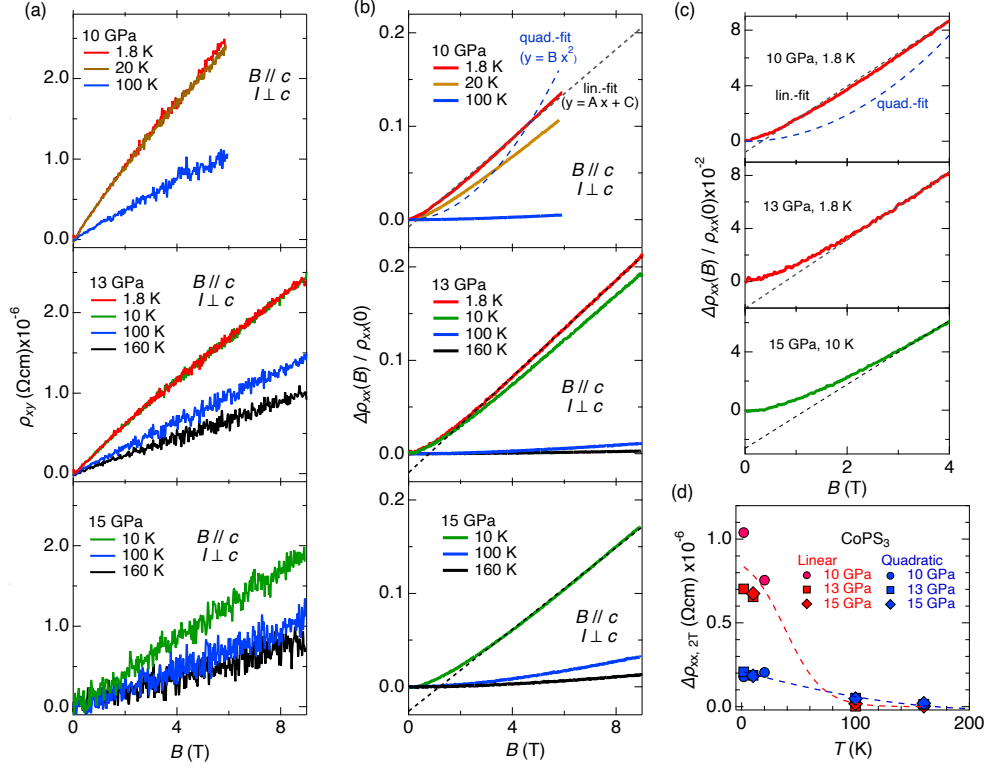


FIG. 6. (color online) Transverse transport data from metallic CoPS<sub>3</sub> at 10, 13, and 15 GPa. (a) The  $\rho_{xx}$  at different temperatures. The data at 1.8 K and 20 K at 10 GPa overlap each other (top panel). The data at 1.8 K and 10 K at 13 GPa overlap (middle panel). (b) The  $\Delta\rho_{xx}(B)/\rho_{xx}(B=0)$ . The dotted (black) and dashed (blue) lines in the top panel indicate the linear fit,  $y = Ax + C$  with  $A = 1.927(3) \times 10^{-3}$ ,  $C = -7.7772(3) \times 10^{-3}$  and quadratic-fits (quad.-fit,  $y = Bx^2$  with  $B = 4.82(4) \times 10^{-3}$ ) to the data at 10 GPa and 1.8 K. (c)  $\Delta\rho_{xx}(B)/\rho_{xx}(B=0)$  at low field. (d) The linear and quadratic components of MR under a field of 2 T for CoPS<sub>3</sub>. The broken lines are guide for eyes.

ally, CDW and SDW are not likely judging from our resistance and XRD measurement results. The curves do not show an abrupt change in the slope of  $\rho_{xx}$  vs.  $T$  that suggests some transition (Fig. 2b). Our XRD measurements does not observe the appearance of satellite peaks, which is suggestive of CDW, in the HP-I phase. Finally, the rapid diminution of  $A(T)$  at elevated temperatures argues against phonon (Umklapp)- [60] or excitation-based [55] scattering mechanisms.

We next test the density fluctuation scenario. Since our sample is under non-hydrostatic stress due to the solid PTM, it is the most straightforward scenario to consider. However, two experimental observations hamper this conclusion. As mentioned, the density fluctuation effects become more prominent in high-mobility and low-carrier density materials [57, 64]. The estimated  $n_{e,av.}$  and  $\mu_{e,av.}$  for CoPS<sub>3</sub> are far bigger and smaller than those materials [57, 67, 68]. The quadratic component in  $\rho_{xx}$  vs.  $B$  becomes more obvious at higher pressures. Since the pressure gradient across the sample generally develops with pressure in a solid PTM, a more amplified density fluctuation and even more linear MR are expected. Therefore, we defer concluding that density fluctuations are the dominant source of LMR in CoPS<sub>3</sub>.

Finally, we consider the spin-disordered mechanism [65, 66]. As discussed above, metallic CoPS<sub>3</sub> is thought to be in the HS/LS Co<sup>2+</sup> mixed state. The presence of remaining magnetic moments implies the presence of short-range magnetic ordering: SRO (*cf.* analysis of the phenomenon in FePS<sub>3</sub> [4]) or some degree of inhomogeneous magnetic moment distribution. Focusing on the latter case, the presence of inhomogeneously distributed magnetic moments will possibly affect the conduction carrier trajectories allowing irregular current paths and the LMR. This interpretation is consistent with the observation that the quadratic component becomes more noticeable in the  $\rho_{xx}$  vs.  $B$  at higher pressure, implying more homogeneous magnetic moment distribution is promoted by pressure (Fig. 6c). Our transverse electrical transport analysis, as well as the crystal structure analysis, support the conclusion that SCO does not complete across the IMT and the magnetic moments persists in the HP-I.

TABLE I. Structural and electronic phase diagram of  $MPS_3$  that metallize via Mott transition.  $AFM_{out}$  and  $AFM_{in}$  mean that the magnetic moments are pointing mostly out-of-plane and in-plane directions, respectively. The  $P_c$  is the pressure where crystal structures start transformations.  $\Delta V$  is the volume reduction at Mott-IMT.

	A.P.	H.P.		Ref. / Note	
$V_{0.9}PS_3$	$C2/m$ ( $\beta\sim 107^\circ$ ) AFM $_{NA}$ <sup>a</sup> , $\mathbf{q} = [010]$ , ins.	$C2/m$ ( $\beta\sim 90^\circ$ ) ins. <sup>b</sup>	met. <sup>c</sup>	[12, 69]	
$P_c$	—	2.6 GPa	12 GPa		
$MnPS_3$	$C2/m$ ( $\beta\sim 107^\circ$ ) AFM $_{out}$ , $\mathbf{q} = [010]or[000]$ , ins.	$P\bar{3}1m$ ins.	$C2/m$ ( $\beta\sim 90^\circ$ ) met.	[13, 19, 70, 71] SCO at 28 GPa	
$P_c$	—	10 GPa	28 GPa, $\Delta V\sim 19.7\%$		
$FePS_3$	$C2/m$ ( $\beta\sim 107^\circ$ ) AFM $_{out}$ , $\mathbf{q} = [01\frac{1}{2}]$ , ins.	$C2/m$ ( $\beta\sim 90^\circ$ ) AFM, $\mathbf{q} = [010]$ , ins.	$P\bar{3}1m$ SRO, met.	[4, 14, 70, 71] SCO at 14 GPa	
$P_c$	—	2 GPa	14 GPa, $\Delta V\sim 10.6\%$		
$CoPS_3$	$C2/m$ ( $\beta\sim 107^\circ$ ) AFM $_{in}$ , $\mathbf{q} = [010]$ , ins.	$P\bar{3}$ met.	[3, 70] this study		
$P_c$	—	7 GPa, $\Delta V\sim 2.4\%$			
$NiPS_3$	$C2/m$ ( $\beta\sim 107^\circ$ ) AFM $_{in}$ , $\mathbf{q} = [010]$ , ins.	$P\bar{3}$ ins.	$P\bar{3}1m$ ins.	$P3m1$ met.	[16, 17, 21, 70]
$P_c$	—	7.2 GPa	15 GPa	23 GPa	
$CdPS_3$	$C2/m$ ( $\beta\sim 107^\circ$ ) ins.	$R\bar{3}$	$R\bar{3}$	[20, 70]	
$P_c$	—	0.25 GPa	8.7 GPa		

<sup>a</sup> N.A.: information Not-Available

<sup>b</sup> ins.: insulator

<sup>c</sup> met.: metal

#### IV. DISCUSSION

Table 1 summarizes the structural and electronic evolution of  $MPS_3$  ( $M = V, Mn, Fe, Co, Ni, Cd$ ) reported from experiments to date. All  $MPS_3$  exhibit  $C2/m$  ( $\beta \sim 107^\circ$ ) to trigonal structural transition when subjected to pressure, resulting in a decrease of their monoclinic angle to  $90^\circ$  as a natural consequence of the inter-layer sliding induced by compression. The Mott-IMT transition commonly occurs when  $MPS_3$  compounds are in the trigonal or  $C2/m$  with  $\beta \sim 90^\circ$  symmetries. Table I tells us that symmetry is not necessarily a decisive factor in determining which electronic character the  $MPS_3$  in question will acquire, i.e. insulating or metallic. For example, in  $V_{0.9}PS_3$  the IMT occurs isostructurally across  $C2/m$  [12]. In contrast,  $NiPS_3$  becomes metallic in  $P3m1$  via two types of trigonal high-pressure phases, including  $P\bar{3}$  where its sister compound  $CoPS_3$  is metallic;  $MnPS_3$  and  $FePS_3$  also metallize in the  $C2/m$  and  $P\bar{3}1m$  symmetries [12, 16, 17, 21]. It is likely that the inter-atomic distances play more crucial roles to scale the Mott-IMT,

as well as SCO. Since the electronic configuration, including the electron orbital hybridization between M and S and P, is different in each  $MPS_3$ , simple scaling by the inter-atomic distance would not be applicable.

The question is how the electronic configuration, magnetism, and structure correlate with each other. We see that  $MPS_3$  compounds, as far as the available experimental data display, can be classified into two groups with respect to their pressure transformations. The first contains  $MnPS_3$  and  $FePS_3$  and exhibits the transformation between symmetries in the group-subgroup relation ( $C2/m \leftrightarrow P\bar{3}1m$ ). We note that these compounds align their magnetic moments mostly in the out-of plane direction. The second group is comprised of  $CoPS_3$  and its sister compound  $NiPS_3$ . These materials have moments aligned largely in-plane. Contrary to the first group, the A.P.-phase and the first high-pressure phase are not in the simple group-subgroup relation. The first high-pressure phases suffers from symmetry lowering against the intuitive expectation that compression brings a system in to a more symmetric and closed-packed structure.

NiPS<sub>3</sub> is an insulator in the  $P\bar{3}$  phase, and the Ni<sup>2+</sup> ions are possibly in HS state. Therefore, the potentially remaining magnetic moments of Co<sup>2+</sup>, and possibly Ni<sup>2+</sup>, are likely to affect the high-pressure phase that succeeds the A.P.-phase under compression.

## V. SUMMARY

We have successfully grown high-quality single crystals of CoSP<sub>3</sub> suitably large enough for conducting various high-pressure experiments. We studied the electrical transport and structural evolution of CoPS<sub>3</sub> under quasi-uniaxial pressure along the layer-stacking direction through electrical resistance, HR, MR, Raman scattering, and XRD measurements. Electrical resistance significantly decreases as the pressure increases, consistent with the increase of the optical reflectivity of the sample. CoPS<sub>3</sub> becomes metallic above 7 GPa, accompanied by a structural change from the ambient pressure (A.P.-phase)  $C2/m$  monoclinic phase to a trigonal  $P\bar{3}$  phase in HP-I. Metallic CoPS<sub>3</sub> shows no superconducting transition in the measured temperature range, down to 2 K. Raman scattering measurements show evidence for a further HP-I  $\rightarrow$  HP-II transition above 18 GPa. The  $C2/m \rightarrow$  HP-I structural transformation induces a 2.4% reduction in  $V_{f.u.}$ , strongly suggesting the observed IMT is a Mott transition. On the other hand, the volume reduction of CoPS<sub>3</sub> is much smaller than the reported volume collapse for the Mn and Fe analogous. The Hall effect data indicate the metallic CoPS<sub>3</sub> is a hole dominant conductor. We observed the LMR in a wide range of magnetic fields. The LMR, as well as the small volume reduction across the structural transition and structural analysis, along with the previous theoretical prediction [29], suggest the HS/LS mixing and inhomogeneous magnetic moment dis-

tribution. By revealing the high-pressure phase and electrical transport property of CoPS<sub>3</sub>, this report summarizes the comprehensive phase diagram of MPS<sub>3</sub> ( $M = \text{V, Mn, Fe, Co, Ni, Cd}$ ) that metallize via Mott transitions. The phase diagram indicates the inter-atomic distance, rather than structural symmetry, playing a crucial role in initiating the pressure-induced SCO and IMT. Comparing the high-pressure phases, we suggest that the potentially remaining magnetic moments of Co<sup>2+</sup>, and possibly Ni<sup>2+</sup>, are likely to affect the high-pressure phase that succeeds the A.P.-phase under compression. Strain applications such as twisting, bending, shearing, and stretching would be interesting subjects for future studies.

## ACKNOWLEDGMENTS

This research is funded by the Gordon and Betty Moore Foundation's EPiQS Initiative, Grant GBMF9069 to D.M. XRD experiments in this study were performed at GSECARS (Sector 13), Advanced Photon Source (APS), Argonne National Laboratory. GSECARS is supported by the National Science Foundation – Earth Sciences (EAR-1634415). This research used resources of the Advanced Photon Source, a U.S. Department of Energy (DOE) Office of Science User Facility operated for the DOE Office of Science by Argonne National Laboratory under Contract No. DE-AC02-06CH11357. Crystal growth and Raman characterization were performed under Air Force Office of Scientific Research (AFOSR) grant LRIR 23RXCOR003 and AOARD-MOST Grant Number F4GGA21207H002. Part of the XRD experiment was supported by COMPRES under NSF Cooperative Agreement EAR-1606856. We thank Dr. Antonio M. dos Santos and Prof. Maik Lang for providing us the DACs for the XRD measurements.

- 
- [1] M. A. Susner, M. Chyasnavichyus, M. A. McGuire, P. Ganesh, and P. Maksymovych, Metal Thio- and Selenophosphates as Multifunctional van der Waals Layered Materials, *Advanced Materials* **29**, 1602852 (2017).
  - [2] M. Zhu, H. Kou, K. Wang, H. Wu, D. Ding, G. Zhou, and S. Ding, Promising functional two-dimensional lamellar metal thiophosphates: synthesis strategies, properties and applications, *Materials Horizons* **7**, 3131 (2020).
  - [3] A. R. Wildes, V. Simonet, E. Ressouche, R. Ballou, and G. J. McIntyre, The magnetic properties and structure of the quasi-two-dimensional antiferromagnet CoPS<sub>3</sub>, *Journal of Physics: Condensed Matter* **29**, 455801 (2017).
  - [4] M. J. Coak, D. M. Jarvis, H. Hamidov, A. R. Wildes, J. A. M. Paddison, C. Liu, C. R. S. Haines, N. T. Dang, S. E. Kichanov, B. N. Savenko, S. Lee, M. Kratochvílová, S. Klotz, T. C. Hansen, D. P. Kozlenko, J.-G. Park, and S. S. Saxena, Emergent Magnetic Phases in Pressure-Tuned van der Waals Antiferromagnet FePS<sub>3</sub>, *Physical Review X* **11**, 011024 (2021).
  - [5] A. R. Wildes, S. J. Kennedy, and T. J. Hicks, True two-dimensional magnetic ordering in MnPS<sub>3</sub>, *Journal of Physics: Condensed Matter* **6**, L335 (1994).
  - [6] A. R. Wildes, V. Simonet, E. Ressouche, G. J. McIntyre, M. Avdeev, E. Suard, S. A. J. Kimber, D. Lançon, G. Pepe, B. Moubaraki, and T. J. Hicks, Magnetic structure of the quasi-two-dimensional antiferromagnet NiPS<sub>3</sub>, *Physical Review B* **92**, 224408 (2015).
  - [7] H.-S. Kim, K. Haule, and D. Vanderbilt, Mott Metal-Insulator Transitions in Pressurized Layered Trichalcogenides, *Physical Review Letters* **123**, 236401 (2019).
  - [8] X. Li, T. Cao, Q. Niu, J. Shi, and J. Feng, Coupling the valley degree of freedom to antiferromagnetic order, *Proceedings of the National Academy of Sciences* **110**, 3738 (2013).
  - [9] P. A. Joy and S. Vasudevan, Magnetism in the layered transition-metal thiophosphates MPS<sub>3</sub> ( $M = \text{Mn, Fe, and Ni}$ ), *Physical Review B* **46**, 5425 (1992).
  - [10] D. Lançon, H. C. Walker, E. Ressouche, B. Oulad-diaf, K. C. Rule, G. J. McIntyre, T. J. Hicks, H. M.

- Rønnow, and A. R. Wildes, Magnetic structure and magnon dynamics of the quasi-two-dimensional antiferromagnet  $\text{FePS}_3$ , *Physical Review B* **94**, 214407 (2016).
- [11] A. R. Wildes, H. M. Rønnow, B. Roesli, M. J. Harris, and K. W. Godfrey, Static and dynamic critical properties of the quasi-two-dimensional antiferromagnet  $\text{MnPS}_3$ , *Physical Review B - Condensed Matter and Materials Physics* **74**, 1 (2006).
- [12] M. J. Coak, S. Son, D. Daisenberger, H. Hamidov, C. R. S. Haines, P. L. Alireza, A. R. Wildes, C. Liu, S. S. Saxena, and J.-G. Park, Isostructural Mott transition in 2D honeycomb antiferromagnet  $\text{V}_{0.9}\text{PS}_3$ , *npj Quantum Materials* **4**, 38 (2019).
- [13] Y. Wang, Z. Zhou, T. Wen, Y. Zhou, N. Li, F. Han, Y. Xiao, P. Chow, J. Sun, M. Pravica, A. L. Cornelius, W. Yang, and Y. Zhao, Pressure-Driven Cooperative Spin-Crossover, Large-Volume Collapse, and Semiconductor-to-Metal Transition in Manganese(II) Honeycomb Lattices, *Journal of the American Chemical Society* **138**, 15751 (2016).
- [14] Y. Wang, J. Ying, Z. Zhou, J. Sun, T. Wen, Y. Zhou, N. Li, Q. Zhang, F. Han, Y. Xiao, P. Chow, W. Yang, V. V. Struzhkin, Y. Zhao, and H.-K. Mao, Emergent superconductivity in an iron-based honeycomb lattice initiated by pressure-driven spin-crossover, *Nature Communications* **9**, 1914 (2018).
- [15] C. R. S. Haines, M. J. Coak, A. R. Wildes, G. I. Lampronti, C. Liu, P. Nahai-Williamson, H. Hamidov, D. Daisenberger, and S. S. Saxena, Pressure-Induced Electronic and Structural Phase Evolution in the van der Waals Compound  $\text{FePS}_3$ , *Physical Review Letters* **121**, 266801 (2018).
- [16] T. Matsuoka, A. Haglund, R. Xue, J. S. Smith, M. Lang, A. M. dos Santos, and D. Mandrus, Pressure-Induced Insulator-to-Metal Transition in Two-Dimensional Mott Insulator  $\text{NiPS}_3$ , *Journal of the Physical Society of Japan* **90**, 124076 (2021).
- [17] X. Ma, Y. Wang, Y. Yin, B. Yue, J. Dai, J. Cheng, J. Ji, F. Jin, F. Hong, J.-T. Wang, Q. Zhang, and X. Yu, Dimensional crossover tuned by pressure in layered magnetic  $\text{NiPS}_3$ , *Science China Physics, Mechanics & Astronomy* **64**, 297011 (2021).
- [18] R. Rao, B. S. Conner, R. Selhorst, and M. A. Susner, Pressure-driven phase transformations and phase segregation in ferrielectric  $\text{CuInP}_2\text{S}_6$ - $\text{In}_4/3\text{P}_2\text{S}_6$  self-assembled heterostructures, *Physical Review B* **104**, 235421 (2021).
- [19] N. C. Harms, H.-s. Kim, A. J. Clune, K. A. Smith, K. R. O'Neal, A. V. Haglund, D. G. Mandrus, Z. Liu, K. Haule, D. Vanderbilt, and J. L. Musfeldt, Piezochromism in the magnetic chalcogenide  $\text{MnPS}_3$ , *npj Quantum Materials* **5**, 56 (2020).
- [20] M. Niu, H. Cheng, X. Li, J. Yu, X. Yang, Y. Gao, R. Liu, Y. Cao, K. He, X. Xie, Q. Shen, M. Lu, L. Wang, T. Yin, and J. Yan, Pressure-induced phase transitions in weak interlayer coupling  $\text{CdPS}_3$ , *Applied Physics Letters* **120**, 233104 (2022).
- [21] N. C. Harms, T. Matsuoka, S. Samanta, A. J. Clune, K. A. Smith, A. V. Haglund, E. Feng, H. Cao, J. S. Smith, D. G. Mandrus, H.-s. Kim, Z. Liu, and J. L. Musfeldt, Symmetry progression and possible polar metallicity in  $\text{NiPS}_3$  under pressure, *npj 2D Materials and Applications* **6**, 40 (2022).
- [22] E. Ressouche, M. Loire, V. Simonet, R. Ballou, A. Stunault, and A. Wildes, Magnetoelectric  $\text{MnPS}_3$  as a candidate for ferrotoroidicity., *Physical Review B* **82**, 100408/1 (2010).
- [23] A. Bhutani, J. L. Zuo, R. D. McAuliffe, C. R. dela Cruz, and D. P. Shoemaker, Strong anisotropy in the mixed antiferromagnetic system  $\text{Mn}_{1-x}\text{Fe}_x\text{PSe}_3$ , *Physical Review Materials* **4**, 034411 (2020).
- [24] A. Wiedenmann, J. Rossat-Mignod, A. Louisy, R. Brec, and J. Rouxel, Neutron diffraction study of the layered compounds manganese selenophosphate ( $\text{MnPSe}_3$ ) and iron selenophosphate ( $\text{FePSe}_3$ ), *Solid State Communications* **40**, 1067 (1981).
- [25] K. C. Rule, G. J. McIntyre, S. J. Kennedy, and T. J. Hicks, Single-crystal and powder neutron diffraction experiments on  $\text{FePS}_3$ : Search for the magnetic structure., *Physical Review B: Condensed Matter and Materials Physics* **76**, 134402/1 (2007).
- [26] K. Ichimura and M. Sano, Electrical conductivity of layered transition-metal phosphorus trisulfide crystals, *Synthetic Metals* **45**, 203 (1991).
- [27] G. Le Flem, R. Brec, G. Ouvard, A. Louisy, and P. Segransan, Magnetic interactions in the layer compounds  $\text{MPX}_3$  ( $M = \text{Mn, Fe, Ni}$ ;  $X = \text{S, Se}$ ), *Journal of Physics and Chemistry of Solids* **43**, 455 (1982).
- [28] G. OUVARD, R. BREC, and J. ROUXEL, SYNTHESIS AND PHYSICAL CHARACTERIZATION OF THE LAMELLAR COMPOUND  $\text{COPSe}_3$ , *COMPTES RENDUS DE L ACADEMIE DES SCIENCES SERIE II* **294**, 971 (1982).
- [29] Y. Gu, S. Zhang, and X. Zou, Tunable magnetism in layered  $\text{CoPS}_3$  by pressure and carrier doping, *Science China Materials* **64**, 673 (2021).
- [30] A. F. May, J. Yan, and M. A. McGuire, A practical guide for crystal growth of van der Waals layered materials, *Journal of Applied Physics* **128**, 051101 (2020).
- [31] H. K. Mao, J. Xu, and P. M. Bell, Calibration of the ruby pressure gauge to 800 kbar under quasi-hydrostatic conditions, *Journal of Geophysical Research* **91**, 4673 (1986).
- [32] C. Prescher and V. B. Prakapenka, DIOPRAS : a program for reduction of two-dimensional X-ray diffraction data and data exploration, *High Pressure Research* **35**, 223 (2015).
- [33] URL\_will\_be\_inserted\_by\_publisher (2022), see the Supplemental Material for XRD images.
- [34] B. Cordero, V. Gómez, A. E. Platero-Prats, M. Revés, J. Echeverría, E. Cremades, F. Barragán, and S. Alvarez, Covalent radii revisited, *Dalton Transactions* , 2832 (2008).
- [35] H.-S. Kim, K. Haule, and D. Vanderbilt, Mott Metal-Insulator Transitions in Pressurized Layered Trichalcogenides, *Physical Review Letters* **123**, 236401 (2019).
- [36] Q. Liu, L. Wang, Y. Fu, X. Zhang, L. Huang, H. Su, J. Lin, X. Chen, D. Yu, X. Cui, J.-W. Mei, and J.-F. Dai, Magnetic order in XY-type antiferromagnetic monolayer  $\text{CoPS}_3$  revealed by Raman spectroscopy, *Physical Review B* **103**, 235411 (2021).
- [37] K. Momma and F. Izumi, VESTA 3 for three-dimensional visualization of crystal, volumetric and morphology data, *Journal of Applied Crystallography* **44**, 1272 (2011).
- [38] L. Savary, Transverse transport, *Nature Physics* **14**, 1073 (2018).
- [39] I. M. Lifshits, M. I. Azbel, and M. I. Kaganov, The Theory of Galvanomagnetic Effects in Metals, *Soviet Physics Jetp-Ussr* **4**, 41 (1957).

- [40] J. M. Ziman, Galvanomagnetic properties of cylindrical fermi surfaces, *Philosophical Magazine* **3**, 1117 (1958).
- [41] J. Wang, A. M. DaSilva, C.-Z. Chang, K. He, J. K. Jain, N. Samarth, X.-C. Ma, Q.-K. Xue, and M. H. W. Chan, Evidence for electron-electron interaction in topological insulator thin films, *Physical Review B* **83**, 245438 (2011).
- [42] Y. Zhao, C.-Z. Chang, Y. Jiang, A. DaSilva, Y. Sun, H. Wang, Y. Xing, Y. Wang, K. He, X. Ma, Q.-K. Xue, and J. Wang, Demonstration of surface transport in a hybrid  $\text{Bi}_2\text{Se}_3/\text{Bi}_2\text{Te}_3$  heterostructure, *Scientific Reports* **3**, 3060 (2013).
- [43] H. Tang, D. Liang, R. L. J. Qiu, and X. P. a. Gao, Two-Dimensional Transport-Induced Linear Magnetoresistance in Topological Insulator  $\text{Bi}_2\text{Se}_3$  Nanoribbons, *ACS Nano* **5**, 7510 (2011).
- [44] C. M. Wang and X. L. Lei, Linear magnetoresistance on the topological surface, *Physical Review B* **86**, 035442 (2012).
- [45] G. M. Gusev, E. B. Olshanetsky, Z. D. Kvon, N. N. Mikhailov, and S. A. Dvoretzky, Linear magnetoresistance in  $\text{HgTe}$  quantum wells, *Physical Review B* **87**, 081311 (2013).
- [46] X. Wang, Y. Du, S. Dou, and C. Zhang, Room Temperature Giant and Linear Magnetoresistance in Topological Insulator  $\text{Bi}_2\text{Te}_3$  Nanosheets, *Physical Review Letters* **108**, 266806 (2012).
- [47] M. Novak, S. Sasaki, K. Segawa, and Y. Ando, Large linear magnetoresistance in the Dirac semimetal  $\text{TlBiSe}_2$ , *Physical Review B* **91**, 041203 (2015).
- [48] T. Liang, Q. Gibson, M. N. Ali, M. Liu, R. J. Cava, and N. P. Ong, Ultrahigh mobility and giant magnetoresistance in the Dirac semimetal  $\text{Cd}_3\text{As}_2$ , *Nature Materials* **14**, 280 (2015).
- [49] Y. Zhao, H. Liu, C. Zhang, H. Wang, J. Wang, Z. Lin, Y. Xing, H. Lu, J. Liu, Y. Wang, S. M. Brombosz, Z. Xiao, S. Jia, X. C. Xie, and J. Wang, Anisotropic Fermi Surface and Quantum Limit Transport in High Mobility Three-Dimensional Dirac Semimetal  $\text{Cd}_3\text{As}_2$ , *Physical Review X* **5**, 031037 (2015).
- [50] J. Feng, Y. Pang, D. Wu, Z. Wang, H. Weng, J. Li, X. Dai, Z. Fang, Y. Shi, and L. Lu, Large linear magnetoresistance in Dirac semimetal  $\text{Cd}_3\text{As}_2$  with Fermi surfaces close to the Dirac points, *Physical Review B* **92**, 081306 (2015).
- [51] C. Shekhar, A. K. Nayak, Y. Sun, M. Schmidt, M. Nicklas, I. Leermakers, U. Zeitler, Y. Skourski, J. Wosnitza, Z. Liu, Y. Chen, W. Schnelle, H. Borrmann, Y. Grin, C. Felser, and B. Yan, Extremely large magnetoresistance and ultrahigh mobility in the topological Weyl semimetal candidate  $\text{NbP}$ , *Nature Physics* **11**, 645 (2015).
- [52] Y. Zhao, H. Liu, J. Yan, W. An, J. Liu, X. Zhang, H. Wang, Y. Liu, H. Jiang, Q. Li, Y. Wang, X.-Z. Li, D. Mandrus, X. C. Xie, M. Pan, and J. Wang, Anisotropic magnetotransport and exotic longitudinal linear magnetoresistance in  $\text{WTe}_2$  crystals, *Physical Review B* **92**, 041104 (2015).
- [53] R. Xu, A. Husmann, T. F. Rosenbaum, M.-L. Saboungi, J. E. Enderby, and P. B. Littlewood, Large magnetoresistance in non-magnetic silver chalcogenides, *Nature* **390**, 57 (1997).
- [54] W. Zhang, R. Yu, W. Feng, Y. Yao, H. Weng, X. Dai, and Z. Fang, Topological Aspect and Quantum Magnetoresistance of  $\beta\text{-Ag}_2\text{Te}$ , *Physical Review Letters* **106**, 156808 (2011).
- [55] A. A. Sinchenko, P. D. Grigoriev, P. Lejay, and P. Monceau, Linear magnetoresistance in the charge density wave state of quasi-two-dimensional rare-earth tritellurides, *Physical Review B* **96**, 245129 (2017).
- [56] Y. Feng, Y. Wang, D. M. Silevitch, J.-Q. Yan, R. Kobayashi, M. Hedo, T. Nakama, Y. A. Enuki, A. V. Suslov, B. Mihaila, P. B. Littlewood, and T. F. Rosenbaum, Linear magnetoresistance in the low-field limit in density-wave materials, *Proceedings of the National Academy of Sciences* **116**, 11201 (2019).
- [57] T. Khouri, U. Zeitler, C. Reichl, W. Wegscheider, N. E. Hussey, S. Wiedmann, and J. C. Maan, Linear Magnetoresistance in a Quasifree Two-Dimensional Electron Gas in an Ultrahigh Mobility  $\text{GaAs}$  Quantum Well, *Physical Review Letters* **117**, 256601 (2016).
- [58] A. A. Abrikosov, Quantum magnetoresistance, *Physical Review B* **58**, 2788 (1998).
- [59] A. A. Abrikosov, Quantum linear magnetoresistance, *Europhysics Letters (EPL)* **49**, 789 (2000).
- [60] R. A. Young, Influence of Localized Umklapp Scattering on the Galvanomagnetic Properties of Metals, *Physical Review* **175**, 813 (1968).
- [61] M. Naito and S. Tanaka, Galvanomagnetic Effects in the Charge-Density-Wave State of  $2\text{H-NbSe}_2$  and  $2\text{H-TaSe}_2$ , *Journal of the Physical Society of Japan* **51**, 228 (1982).
- [62] J. C. W. Song, G. Refael, and P. A. Lee, Linear magnetoresistance in metals: Guiding center diffusion in a smooth random potential, *Physical Review B* **92**, 180204 (2015).
- [63] M. M. Parish and P. B. Littlewood, Non-saturating magnetoresistance in heavily disordered semiconductors, *Nature* **426**, 162 (2003).
- [64] J. Hu and T. F. Rosenbaum, Classical and quantum routes to linear magnetoresistance, *Nature Materials* **7**, 697 (2008).
- [65] B. Raquet, M. Viret, P. Warin, E. Sondergard, and R. Mamy, Negative high field magnetoresistance in 3d ferromagnets, *Physica B: Condensed Matter* **294-295**, 102 (2001).
- [66] Q. Wang, W. Zhang, W. Chen, Y. Xing, Y. Sun, Z. Wang, J.-W. Mei, Z. Wang, L. Wang, X.-C. Ma, F. Liu, Q.-K. Xue, and J. Wang, Spin fluctuation induced linear magnetoresistance in ultrathin superconducting  $\text{FeSe}$  films, *2D Materials* **4**, 034004 (2017).
- [67] W. Pan, J. S. Xia, H. L. Stormer, D. C. Tsui, C. L. Vicente, E. D. Adams, N. S. Sullivan, L. N. Pfeiffer, K. W. Baldwin, and K. W. West, Quantization of the Diagonal Resistance: Density Gradients and the Empirical Resistance Rule in a 2D System, *Physical Review Letters* **95**, 066808 (2005).
- [68] S. H. Simon and B. I. Halperin, Explanation for the resistivity law in quantum hall systems, *Physical Review Letters* **73**, 3278 (1994).
- [69] G. Ouvrard, R. Fréour, R. Brec, and J. Rouxel, A mixed valence compound in the two dimensional  $\text{MPS}_3$  family:  $\text{V}_{0.78}\text{PS}_3$  structure and physical properties, *Materials Research Bulletin* **20**, 1053 (1985).
- [70] G. Ouvrard, R. Brec, and J. Rouxel, Structural determination of some  $\text{MPS}_3$  layered phases ( $\text{M} = \text{Mn}, \text{Fe}, \text{Co}, \text{Ni}$  and  $\text{Cd}$ ), *Materials Research Bulletin* **20**, 1181 (1985).
- [71] M. J. Coak, D. M. Jarvis, H. Hamidov, C. R. Haines, P. L. Alireza, C. Liu, S. Son, I. Hwang, G. I. Lampronti, D. Daisenberger, P. Nahai-Williamson, A. R.



Wildes, S. S. Saxena, and J. G. Park, Tuning dimensionality in van-der-Waals antiferromagnetic Mott insu-

lators  $\text{TMPS}_3$ , Journal of Physics Condensed Matter **32**, 124003 (2020).